Beam distortion detection and deflectometry measurements of gigahertz surface acoustic waves

Julien Higuet, Tony Valier-Brasier, Thomas Dehoux, and Bertrand Audoin
*Département d'Acoustique Physique, Université de Bordeaux, CNRS, UMR 5295, I2M,
Talence F-33405, France*

Gigahertz acoustic waves propagating on the surface of a metal halfspace are detected using different all-optical detection schemes, namely, deflectometry and beam distortion detection techniques. Both techniques are implemented by slightly modifying a conventional reflectometric setup. They are then based on the measurement of the reflectivity change but unlike reflectometric measurements, they give access to the sample surface displacement. A semi-analytical model, taking into account optical, thermal, and mechanical processes responsible for acoustic waves generation, allows analyzing the physical content of the detected waveforms. © *2011 American Institute of Physics*. [doi:10.1063/1.3660193]

I. INTRODUCTION

Since the first works by Lord Rayleigh in 1885, the propagation of surface acoustic waves (SAWs) on the free surface of an elastic halfspace have been largely studied. These waves are of great interest for many applications such as seismology, nondestructive testing and evaluation or acoustic microscopy. Many theoretical studies of the propagation of SAWs on anisotropic halfspaces[1] or of the interaction of SAWs with defects[2,3] have therefore been led. High frequency SAWs (from hundreds of MHz to few tens of GHz (Refs. 4 and 5)) appear of great interest for signal processing in telecommunication, or for nondestructive testing in order to scan surfaces or to detect surface or subsurface defects. In this context, a particular attention is directed towards the generation/reception of SAWs by noninvasive laser techniques. High frequency SAWs can be generated in the thermo-elastic or ablation regime using focused laser pulses,[6] transient optical gratings,[7] or metallic nanopattern[8] for photoelastic transduction. However, there is an important need to develop simple and efficient techniques which are able to measure properties of these waves.

Laser-ultrasonic (LU) techniques are powerful tools for the generation and the detection of acoustic waves. Both theoretical and experimental aspects of the generation and detection by nanosecond laser pulses have been extensively studied for more than thirty years. Numerous works are now considering picosecond LU techniques,[9] allowing the generation of higher acoustic frequencies (up to THz) and better spatial resolution thanks to shorter femtosecond laser pulses and tighter focusing. Picosecond LU techniques are based on pump-probe setups. A pump laser pulse is absorbed by the sample and generates acoustic waves via photothermal and thermomechanical couplings. A time-delayed probe pulse interacts with the sample surface, and the probe light reflected by the sample is analyzed, providing information on the generated acoustic waves.

Among the different optical detection schemes, reflectometric and interferometric techniques are the most used to study the picosecond SAWs. Reflectometry allows the measurement of changes in the intensity of the probe pulse after reflection on the sample. This technique is not directly sensitive to the surface displacement,[10] but has recently allowed measurements of the strain induced by SAWs propagation by taking advantage of optical birefringence.[11] Interferometric techniques measure both the amplitude and phase of the optical reflectivity change and is directly sensitive to the normal displacement of the sample surface. Picosecond time scale measurements of SAWs have been carried out using different interferometric setup such as Michelson[12] or Sagnac-based.[13] If both reflectometry and interferometry are mature and experienced techniques, they both have limitations in the purpose of SAWs detection: reflectometry requires strong photoelastic coefficient; implementation of interferometry is demanding in terms of stability and alignment sensitivity.

In this paper, we demonstrate the suitability of alternative experimental setups to detect high frequency surface displacement while keeping the simplicity of reflectometric measurement. The first detection scheme, called deflectometry, has been widely used for more than 20 years[14,15] to detect MHz acoustic waves generated by nanosecond laser pulses. This technique is based on the measurement of the variation of the probe beam direction after reflection on the sample surface: as a surface wave propagates, the sample surface undulates, causing the probe laser beam to be deflected. The second approach, the beam distortion detection (BDD) technique,[16] has been recently developed. This technique is based on the measurement of the probe beam radius changes. Because of the acoustic-induced local change in the surface curvature, the optical probe beam radius is modified after reflection on the sample. Although these techniques seem accurate candidates to measure SAWs, only very few experiments have been carried out in picosecond ultrasonics.[4] Thorough study of high frequency SAWs, using these two experimental techniques, have been performed and analyzed with semi-analytical calculations.

In the following (Sec. II), the experimental setup and time resolved measurements of SAWs using the above-mentioned detection techniques are first presented. Then, in Sec. III, a

82, 114905-1

semi-analytical model taking into account the photothermal generation and the thermo-acoustic coupling is developed in order to describe the generation and the propagation of the elastic waves in a semi-infinite medium. This model is based on analytical calculations of the temperature and displacement fields in the Fourier domain. Finally (Sec. IV), the experimental signals detected by deflectometry and BDD are interpreted with the help of the semi-analytical model.

II. EXPERIMENTS

A. Optical measurement of gigahertz surface acoustic waves

The pump-probe setup is described in Fig. 1. Laser pulses of 100 fs duration, with a central wavelength $\lambda \approx 800$ nm, are generated by a Ti:sapphire oscillator. The laser beam is split using a polarizing beam splitter (PBS1 in Fig. 1) to provide synchronous pump and probe pulse trains of repetition frequency 82 MHz. Probe pulses are time-delayed with respect to pump pulses (up to 6 ns) by a motorized delay line in order to measure the time-resolved reflectivity change of the sample. Both pump and probe beams are focused on the sample by a $\times 100$ (N.A. 0.8) microscope objective allowing a focus spot size close to the diffraction limit.

Linearly polarized pump pulses are partially absorbed and create a localized and prompt heating of the sample. The ensuing thermal expansion generates acoustic waves via thermo-elastic coupling. Modeling of this opto-acoustic transduction process is detailed in Sec. III. The pump beam is modulated at a frequency $f_m = 330$ kHz by an acousto-optical modulator to provide reference for lock-in amplification. In order to decrease the focus spot size on the sample, and hence generate higher frequency acoustic waves, pump pulses are frequency-doubled in a β-barium borate crystal ($\lambda_{\text{pump}} \approx 400$ nm). The incident pump power is approximately 200 μW on the sample.

After reflection on the sample surface, the circularly polarized probe beam is focused by a collecting lens on a photodiode, the output of which is lock-in amplified. The probe power on the sample surface (approximately 20 μW) is set to ensure a linear response of the photodiode. The relative
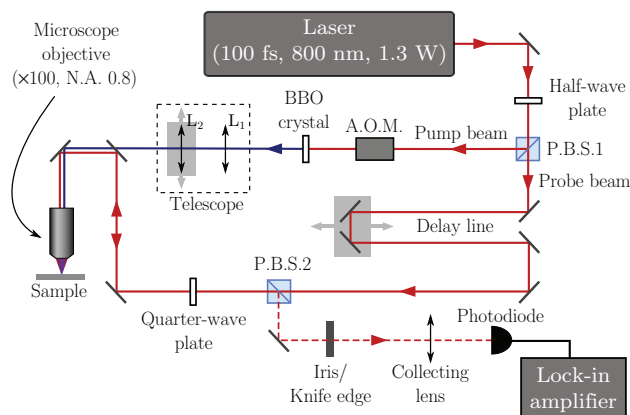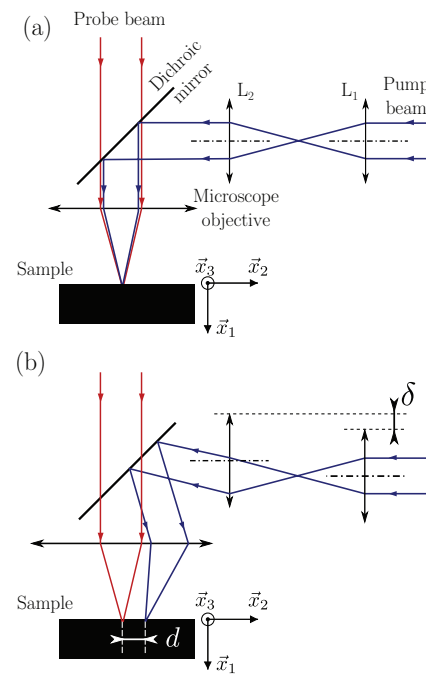

FIG. 2. (Color online) Displacement of the pump focus on the sample surface. (a) When the two lenses of the telescope L_1 and L_2 are aligned, pump and probe spots are superimposed on the sample. (b) Shifting transversally L_2 by δ separates the generation and detection points by a distance d.

variation of photodiode output tension $\Delta V/V$ is therefore proportional to the relative variation of the sample reflectivity $\Delta R/R$.

The $1/e$ radius of the pump and probe spot sizes are measured from the intensity profiles recorded by a CCD camera at ≈ 400 nm and 800 nm, respectively.

In order to study the propagation of SAWs, the distance d between pump and probe spots on the sample surface can be increased (see Fig. 2). The pump beam passes through a confocal telescope: translating transversally one of the lens of the telescope (labeled L_2) modifies the direction of the pump beam and consequently the position of the pump spot on the sample. L_2 is mounted on a motorized translation stage which allows tuning distance d up to about 6 μm.

Three different measurements can be carried out with this experimental setup. The first technique is a conventional measurement of the real part of the photo-induced reflectivity change as a function of the pump-probe delay Δt (reflectometry measurement). This measurement provides access to the in-depth strain and temperature fields.[10] However, probing of the surface displacement, and in particular of surface waves, is not possible.

In the second technique, called deflectometry, a knife edge is placed in front of the collecting lens (Fig. 3(a)). This knife edge is centered to transmit 50% of the probe power when the sample is not excited. The spatial wavelength of the generated SAWs is comparable with the probe spot size on the sample. In this configuration, probe beam optical diffraction due to the surface deformation is negligible and we consider that the probe beam reflection can be described by the geometrical optics.[17–19] The probe beam deflection modifies the probe power shadowed by the knife edge, thus transmitted to the photodiode. In the case of small surface

FIG. 1. (Color online) Pump-probe setup used for the generation and the detection of surface acoustic waves.
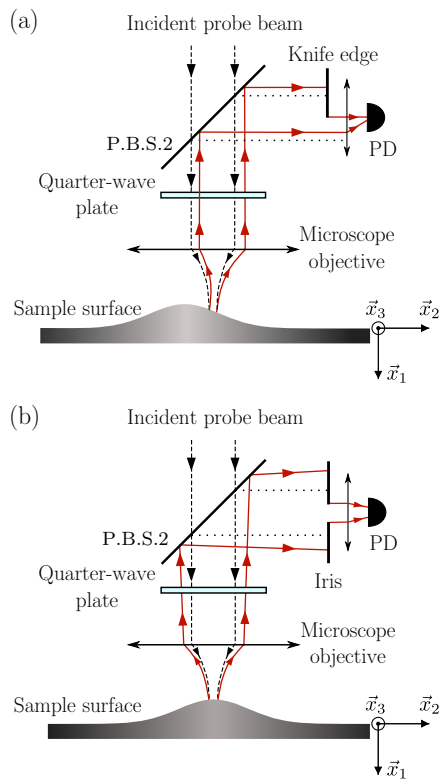
FIG. 3. (Color online) (a) Principle of deflectometry. Because of the surface displacement, the direction of the reflected probe beam (plain line) is modified. The probe power transmitted to the photodiode (PD) changes due to the clipping of the beam by the knife edge. The dotted line stands for the probe beam when reflected on a plane (non excited) surface. (b) Principle of the BDD technique. The wavefront of the incident probe beam (dashed black line) is modified after reflection on the sample (plain red line). The probe power measured by the photodiode changes due to the clipping of the beam by the iris.

displacement (typically of few picometers with a femtosecond laser thermoelastic source) compared to the acoustic wavelength, the power variation on the photodiode is directly proportional to the surface slope[17] $\partial u_1/\partial x_2$ at the center of the probe spot, u_1 being the surface normal displacement along the x_1 axis (see Fig. 2 for axis definition). Owing to axial symmetry of the source, the surface slope is always zero at the generation point. Consequently, it is necessary to separate generation and detection spots to measure a non-zero deflectometric contribution.

The third technique is referred to as the beam distortion detection (BDD) technique.[16] An iris is inserted before the collecting lens and the photodiode and is centered to maximize the probe power transmission. The displacement of the sample surface modifies the wavefront of the probe beam after reflection and consequently the size of the probe beam on the iris plane (see Fig. 3(b)). Since the surface displacement is small compared to the probe beam optical wavelength ($\lambda \approx 800$ nm), the variation of the probe beam power transmitted by the iris is directly proportional to the normal displacement of the surface u_1. In order to maximize the sensitivity to beam distortion, the average iris transmission is set to $\approx 65\%$.[16]

Note that both BDD and deflectometry techniques allow access to the surface displacement (or its spatial derivative), but also contain photothermal and photoelastic contri-

butions as they both result from modified reflectometry measurements.

B. Time resolved measurements

Measurements using these three different techniques have been carried out on a semi-infinite titanium alloy sample (Ti6Al4V) of density $\rho = 4500$ kg m^{-3}. Thermal and optical parameters of this sample are taken from Ref. 20: thermal conductivity $\kappa = 21.9$ W m^{-1}K^{-1}, specific heat capacity $C_p = 500$ J kg^{-1}m^{-3}, thermal dilatation coefficient $\alpha = 9 \times 10^{-6}$ K^{-1}, and refractive index $n = 1.55 + 2.15j$ at 400 nm.

For all measurements presented in this paper, a specific attention has been paid to the position of the sample surface with respect to the probe beam waist. Indeed, the contribution of the beam distortion to the reflectivity change is zero when the sample is exactly at the probe waist position, and it presents two maxima (with opposite signs) at specific positions above and below this waist position.[16] When setting the sample to any of these optimum positions, a non-zero contribution of the beam distortion to the reflectivity change arises, even without an iris in the optical path, because of the clipping of the reflected probe beam by the microscope objective. The sample position has then been set to about 1 μm above the probe focus in order to measure no beam distortion contribution when there is no iris in front of the photodiode, and to measure a non-zero BDD signal with the iris.

Figure 4 shows comparison between the relative variation of photodiode voltages $\Delta V/V$ (in phase with pump modulation) measured with the different techniques. $\Delta V/V$ for negative delays has been set to zero to remove the photothermal contribution to the reflectivity change at the pump modulation frequency f_m.[21]

When pump and probe are superimposed (Fig. 4(a)), the optical reflectivity measured with the classical reflectometric technique undergoes a sudden change at $\Delta t = 0$ (temporal synchronization of pump and probe pulses), due to the absorption of the pump pulses by conduction electrons in Ti. This electronic absorption takes place on a picosecond time scale, and is followed by a slower reflectivity decay due to the nanosecond time scale thermalization of the lattice. Because of the axial symmetry of the pump spot, the deflection of the probe beam is zero when the pump-probe distance is $d = 0$. $\Delta V/V$ measured by the deflectometry technique (not shown in Fig. 4(a)) is therefore equal to $\Delta V/V$ measured by the reflectometry technique. With the same experimental conditions, $\Delta V/V$ measured by the BDD technique shows a similar behavior. However, a clear contribution of the probe defocusing caused by the surface displacement is observed for pump-probe delays between 150 ps and 750 ps (with a maximum contribution around 350 ps).

In Fig. 4(b), BDD and deflectometry measurements are compared for a pump-probe distance $d = 4.1$ μm. For a clearer comparison, Gaussian averaging over a ≈ 30 ps duration window has been added for both data sets and BDD measurement has been multiplied by two in order to have an amplitude similar to that of deflectometry measurement.[22] For this pump-probe distance d, the nanosecond time scale photothermal contribution to the reflectivity change is
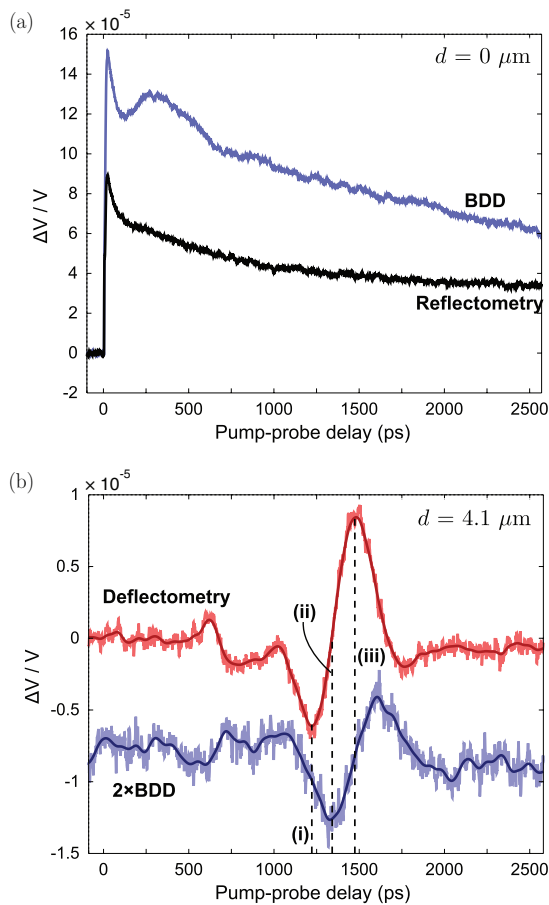
FIG. 4. (Color online) Relative variation of the photodiode voltage after lock-in amplification measured with the different techniques (reflectometry, BDD, and deflectometry) in a Ti alloy sample. (a) Reflectometry (bottom) and BDD measurements (top) when pump and probe beams are superimposed on the sample. (b) Comparison between deflectometry measurement (top) and 2×BDD measurement (bottom) when generation and detection are separated by $d = 4.1$ μm. For a clearer comparison, BDD measurement (bottom) has been vertically shifted and Gaussian smoothing of both BDD and deflectometry data sets have been added.

negligible as d is greater than the sum of the pump radius and the thermal diffusion length $\mu = \sqrt{\kappa / \rho C_p \pi f}$ $= 0.2$ μm at the repetition frequency f of pump pulses. On both measurements, the observed variation of $\Delta V / V$ is therefore associated to the propagation of SAWs. These variations are different according to the detection technique used. In particular, for delays between 1 and 2 ns, the deflectometry measurement is similar to the temporal derivative of the BDD measurement: it is zero when the BDD signal is minimum (see vertical dashed lines (ii) in Fig. 4(b)), and has a local maximum when the BDD signal has a point of inflection (see vertical dashed lines (i) and (iii)).

The signals presented in Fig. 4(b) contain contributions of different SAWs, notably Rayleigh and skimming waves, which can potentially overlap. To identify these contributions and to explain the difference in the shape of $\Delta V / V$ measured by deflectometry and BDD, a semi-analytical model has been developed. This model describes the generation and propagation of elastic waves in a semi-infinite medium, taking into account the transient optical, thermal, and mechanical processes occurring in the sample.

III. SEMI-ANALYTICAL CALCULATIONS OF ACOUSTIC WAVEFORMS

Several modelings of the generation of elastic waves in an anisotropic halfspace by transient point or line sources have been developed.[23,24] The purpose here is to take into account the excitation of the elastic waves by a photothermal process. The localized photoinduced temperature rise caused by the pump laser in the medium, induces a thermal dilatation which leads to the generation of elastic waves by thermo-elastic coupling. Thus, the modeling is based on the description of the evolutions of the temperature field in the medium and of the elastic displacement.

A. Coupled temperature diffusion and acoustic propagation equations

A semi-infinite anisotropic viscoelastic medium of density ρ occupies the region $x_1 \geq 0$ with a plane surface located at $x_1 = 0$ in cartesian coordinates (x_1, x_2, x_3) (see Fig. 2). The origin is chosen to coincide with the center of the pump laser spot at the free surface of the sample. The absorption of the radiation of this incident pump laser leads to a sudden localized temperature rise of the sample. Assuming the temperature field is not affected by elastic waves, the photoinduced temperature rise T is described by the heat conduction equation,

$$\rho C_p \frac{\partial T}{\partial t} = \nabla(\overline{\overline{\kappa}} : \nabla T) + Q, \tag{1}$$

where Q is the source term corresponding to the absorption of the pump laser beam and $\overline{\overline{\kappa}}$ the tensor of heat conductivity.

The displacement field **u** is solution of the equation of motion,

$$\rho \frac{\partial^2 \mathbf{u}}{\partial t^2} = \text{div}\overline{\overline{\sigma}}, \tag{2}$$

where the components σ_{ij} of the stress tensor $\overline{\overline{\sigma}}$ are given by[25]

$$\sigma_{ij} = \tilde{C}_{ijkl} \frac{\partial u_k}{\partial x_l} - \lambda_{ij} T \delta_{ij}. \tag{3}$$

The components of the viscoelasticity tensor $\tilde{C}_{ijkl}$ are given by a Kelvin-Voigt model[26] and the tensor $\overline{\overline{\lambda}}$ is the product of the viscoelasticity tensor and the thermal rigidity tensor $\overline{\overline{\alpha}}$. It is worth noting that the thermal stress is the source term of Eq. (2).

B. Solutions in the frequency domain

Equations (1) and (2) can be solved simultaneously in the frequency-wavelength domain using a triple inverse Fourier transform,

$$f(x_1, x_2, x_3, t) = \frac{1}{(2\pi)^3} \int_{-\infty}^{+\infty} \int_{-\infty}^{+\infty} \int_{-\infty}^{+\infty}$$
$$\times \hat{f}(x_1, k_2, k_3, \omega) e^{j(\omega t - k_2 x_2 - k_3 x_3)} dk_2 dk_3 d\omega, \tag{4}$$

where f stands for either **u** or T. In the remainder, the hat grapheme denotes functions defined in the dual space.

However, for transversely isotropic media with a symmetry plane parallel to the boundary ($x_1 = 0$), the cylindrical symmetry of the problem allows calculation of the spatiotemporal evolution of the normal displacement u_1 at a position ($x_1, x_2, x_3 = 0$) by a double Fourier-Hankel transform,[27]

$$u_1(x_1, x_2, t) = \frac{1}{(2\pi)^2} \int_{-\infty}^{+\infty} \int_{0}^{+\infty}$$
$$\times \hat{u}_1(x_1, k_2, \omega) J_0(-k_2 x_2) e^{j\omega t} k_2 \, dk_2 \, d\omega, \tag{5}$$

where J_0 stands for the zero-order Bessel function of the first kind.[28] The same scheme can be applied to the other components of the displacement, using convenient Bessel functions.[27]

The source term corresponding to the Gaussian pump laser beam propagating at normal incidence in direction x_1 takes the following form:

$$Q(x_1, x_2, t) = \beta I_0 (1 - R) G_\chi(x_2) G_\tau(t) e^{-\beta x_1}, \tag{6}$$

where I_0 is the incident energy per unit surface, R is the coefficient of the optical intensity reflection at the air/medium interface for a wave propagating in air, G_χ is the lateral distribution intensity, and G_τ is the laser pulse intensity in time. Gauss functions of full width at half maximum (FWHM) χ and τ are assumed for G_χ and G_τ, respectively, with

$$G_a(x) = \frac{1}{a} \sqrt{\frac{4\ln(2)}{\pi}} e^{-4\ln(2)\frac{x^2}{a^2}}, \tag{7}$$

where a represents a FWHM ($a = \chi, \tau$).

The heat flux proportionnal to $\partial T/\partial x_1$ vanishes on the surface $x_1 = 0$, meaning that the temperature field satisfies a Neumann boundary condition on the free surface. The heat diffusion Eq. (1) in the dual space (ω, k_2) being a second order differential equation, taking into account the Neumann boundary condition yields the solution

$$\hat{T}(x_1) = \sum_{q=\beta,\Gamma} \frac{\beta I_0 (1 - R)}{\kappa(\Gamma^2 - \beta^2)} \hat{T}^q e^{-q x_1}, \tag{8}$$

with

$$\Gamma = \sqrt{j\omega \frac{\rho C_p}{\kappa} + k_2^2}, \tag{9}$$

and

$$\begin{cases} \hat{T}^\beta = 1, \\ \hat{T}^\Gamma = -\beta/\Gamma. \end{cases} \tag{10}$$

In the dual space (ω, k_2), the vectorial equation of motion (2) is a system of two second order differential linear equations with source terms,

$$\begin{cases} \left(\rho\omega^2 - k_2^2 \tilde{C}_{66}\right) \hat{u}_1 + \tilde{C}_{11} \frac{\partial^2 \hat{u}_1}{\partial x_1^2} \\ \quad - jk_2(\tilde{C}_{12} + \tilde{C}_{66}) \frac{\partial \hat{u}_2}{\partial x_1} = \lambda_{11} \frac{\partial \hat{T}}{\partial x_1}, \\ \left(\rho\omega^2 - k_2^2 \tilde{C}_{22}\right) \hat{u}_2 + \tilde{C}_{66} \frac{\partial^2 \hat{u}_2}{\partial x_1^2} \\ \quad - jk_2(\tilde{C}_{12} + \tilde{C}_{66}) \frac{\partial \hat{u}_1}{\partial x_1} = -jk_2 \lambda_{22} \hat{T}. \end{cases} \tag{11}$$

The solution of this system is the sum of a homogeneous solution and of a particular solution. Each component of the spectrum of the homogeneous solution is expressed as a plane wave, $\hat{\mathbf{U}}^h = (\hat{U}_1, \hat{U}_2) \exp(-jk_1 x_1)$, where k_1 is the projection of the wavevector in direction $\vec{x}_1$, leading to the eigenvalues problem

$$\begin{pmatrix} \rho\omega^2 - k_2^2 \tilde{C}_{66} - k_1^2 \tilde{C}_{11} & -k_1 k_2(\tilde{C}_{12} + \tilde{C}_{66}) \\ -k_1 k_2(\tilde{C}_{12} + \tilde{C}_{66}) & \rho\omega^2 - k_2^2 \tilde{C}_{22} - k_1^2 \tilde{C}_{66} \end{pmatrix}$$
$$\times \begin{pmatrix} \hat{U}_1 \\ \hat{U}_2 \end{pmatrix} = \begin{pmatrix} 0 \\ 0 \end{pmatrix}. \tag{12}$$

The solving of Eq (12) leads to the determination of the eigenvalues $(k_1^n)^2$, where k_1^n and $-k_1^n$ stand for propagating and counterpropagating waves, respectively, and where $n = L$, T stands for the longitudinal and transverse bulk waves, respectively. The medium being a halfspace set in the region $x_1 \geq 0$, only waves with energy propagating in the direction of increasing x_1 are considered. The vectors associated to the eigenvalues (k_1^n) are expressed as

$$\begin{pmatrix} \hat{U}_1^n \\ \hat{U}_2^n \end{pmatrix} = \begin{pmatrix} \rho\omega^2 - k_2^2 \tilde{C}_{22} - (k_1^n)^2 \tilde{C}_{66} \\ k_1^n k_2(\tilde{C}_{12} + \tilde{C}_{66}) \end{pmatrix}. \tag{13}$$

The spectrum of the displacement field is expressed as

$$\hat{\mathbf{U}} = \sum_{q=\beta,\Gamma} \hat{\mathbf{U}}^q e^{-q x_1} + \sum_{n=L,T} \hat{\mathbf{U}}^n \hat{\zeta}^n e^{-jk_1^n x_1}, \tag{14}$$

where the coefficients $\hat{\zeta}^n$ are the amplitude of the bulk waves ($n = L, T$). The terms $\hat{\mathbf{U}}^\beta$ and $\hat{\mathbf{U}}^\Gamma$ are the amplitude vectors of the particular solutions resulting from the optical absorption and of the thermal stress, respectively. These amplitude vectors are obtained by replacing the displacement field $\hat{u}(x_1)$ by each particular solution $\hat{\mathbf{U}}^q e^{-q x_1}$ in the system (11).

The normal stress σ_{11} and the tangential stress σ_{12} on the free surface $x_1 = 0$ are expressed as

$$\begin{cases} \hat{\sigma}_{11} = -\sum_{q=\beta,\Gamma} \left[q\tilde{C}_{11} \hat{U}_1^q + j\tilde{C}_{12} k_2 \hat{U}_2^q + \lambda_{11} \hat{T}^q \right] \\ \quad - j \sum_{n=L,T} A^n \hat{\zeta}^n, \\ \hat{\sigma}_{12} = \tilde{C}_{66} \sum_{q=\beta,\Gamma} \left[q\hat{U}_2^q - jk_2 \hat{U}_1^q \right] - \sum_{n=L,T} B^n \hat{\zeta}^n, \end{cases} \tag{15}$$

where

$$\begin{cases} A^n = \tilde{C}_{11} k_1^n \hat{U}_1^n + \tilde{C}_{12} k_2 \hat{U}_2^n, \\ B^n = j\tilde{C}_{66} \left(k_2 \hat{U}_1^n + k_1^n \hat{U}_2^n \right). \end{cases} \tag{16}$$

Vanishing of both normal and tangential stresses on the free surface ($x_1 = 0$) leads to the expressions of the amplitudes

of longitudinal (ζ^L) and transverse (ζ^T) bulk waves,

$$\begin{pmatrix} \zeta^L \\ \zeta^T \end{pmatrix} = \begin{pmatrix} j A^L & j A^T \\ B^L & B^T \end{pmatrix}^{-1}$$

$$\begin{pmatrix} -\sum_{q=\beta,\Gamma} \left[q\tilde{C}_{11}\hat{U}_1^q + j\tilde{C}_{12}k_2\hat{U}_2^q + \lambda_{11}\hat{T}^q \right] \\ \tilde{C}_{66}\sum_{q=\beta,\Gamma} \left[q\hat{U}_2^q - jk_2\hat{U}_1^q \right] \end{pmatrix}. \qquad (17)$$

The spatiotemporal evolution of the normal displacement u_1 is calculated from the amplitude of bulk waves (ζ^n) in the (ω, k_2) space using a numerical inverse Fourier transform (5). The determinant of Eq. (17) contains fundamental information on the waves generated in the medium. Zeros correspond to poles or branch points in the complex plane. To preserve the influence of those singularities and avoid numerical divergence altogether, a numerical technique based on a complex frequency is used in order to calculate the inverse Fourier transform.[29]

IV. DISCUSSION

In this section, the semi-analytical calculations presented in Sec. III are compared to reflectivity change measurements in order to identify the contributions of the different generated SAWs.

A. SAWs probed by deflectometry

Figure 5 shows normalized deflectometry signals and theoretical calculations of the spatial derivative of the surface displacement $\partial u_1/\partial x_2$, for pump-probe distances varying from d = 2.5 μm to d = 4.4 μm. Experimental and semi-analytical
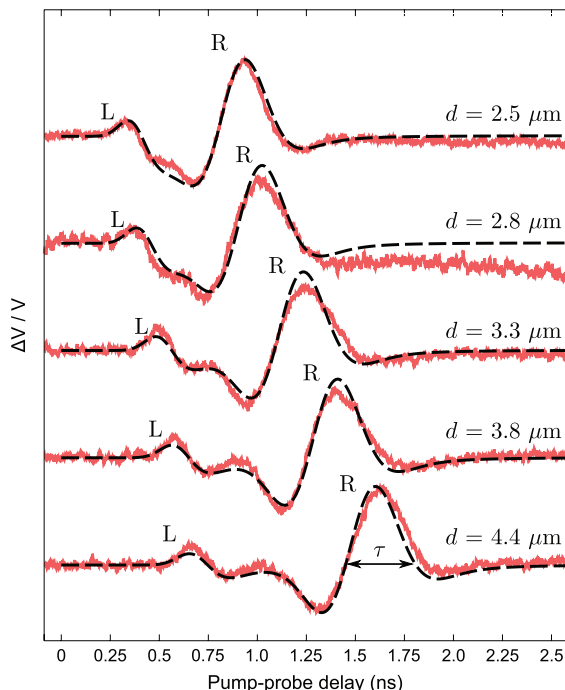

FIG. 5. (Color online) Comparison between deflectometry measurements (red plain lines) and calculations of $\partial u_1/\partial x_2$ (black dashed lines) for pump-probe distances varying from d = 2.5 μm to d = 4.4 μm.

results are normalized (peak-to-peak amplitude set to 1). Remarkable agreement is observed between experimental results and calculations for every pump-probe distance d.

For these calculations, the components of the viscoelasticity tensor are identified by fitting numerical results to experimental data. We chose an isotropic symmetry with the independent components of the elasticity tensor C_{11} = 176 GPa and C_{44} = 41 GPa (in good agreement with previously reported values[30]). The viscoelastic dissipation is taken into account in the modeling through a Kelvin-Voigt model in space (ω, k_2), $\tilde{\overline{\overline{C}}} = \overline{\overline{C}} + j\omega\overline{\overline{\eta}}$, where $\overline{\overline{\eta}}$ is a tensor of viscosity. The independent components of the dynamic viscosity tensor are η_{11} = 0.88 Pa s and η_{44} = 0.2 Pa s. The knowledge of the components of the elasticity tensor allows estimating the longitudinal bulk waves velocity V_L = 6250 m/s and the Rayleigh wave velocity V_R = 2820 m/s. For each pump-probe distance d, excellent agreement is observed.

Two acoustic waves are clearly identified by their time of flight on Fig. 5, the faster being the skimming longitudinal wave (marked L) and the slowest being the Rayleigh surface wave (marked R).[31] From the Rayleigh pulse half temporal period τ (see Fig. 5), the central frequency of the Rayleigh wave is calculated at $f_R = 1/2\tau = 1.7$ GHz. From this frequency, the calculated acoustic wavelength λ_R is 1.7 μm, close to twice the pump spot size on the sample surface ($\approx$1.6 μm).

Thanks to this modeling, we identify the Rayleigh surface wave in Fig. 4(b) for delay close to 1.5 ns. The Rayleigh wave being non-dispersive, its temporal and spatial derivative are proportional $V_R \times \partial u_1/\partial x_2 = \partial u_1/\partial t$. This explains the phase shift observed on Fig. 4(b) between BDD and deflectometry measurements, confirming that deflectometry measurement is indeed proportional to the spatial (and temporal in this case) derivative of the BDD measurement.

Pump-probe distances considered for Fig. 5 are high enough to avoid any photothermal contribution to $\Delta V/V$. Such a contribution is observed in Fig. 6 where d is set to 0.9 μm. On the raw deflectometry measurement (see inset of Fig. 6), the photothermal and SAWs contributions are of the same order of magnitude, preventing from clearly identifying skimming and Rayleigh waves. However, one can remove the photothermal contribution by subtracting a reflectometry measurement from the raw deflectometry measurement. The so-corrected deflectometry measurement is presented in the main plot in Fig. 6. Skimming and Rayleigh waves are now clearly observable, the agreement between measured data and calculated $\partial u_1/\partial x_2$ being very good. A slight discrepancy is observed between the measured and calculated relative amplitudes of the skimming wave compared to that of the Rayleigh wave. This difference could be due to a deflection of the probe beam caused by a temperature gradient[18] (and hence a refractive index gradient) on the probe focus point, this gradient being negligible for d greater than the thermal diffusion length.

B. SAWs probed by the BDD technique

Similar comparisons have been carried out between BDD measurements and calculation of the normal displacement u_1 of the surface, using the titanium alloy properties found in
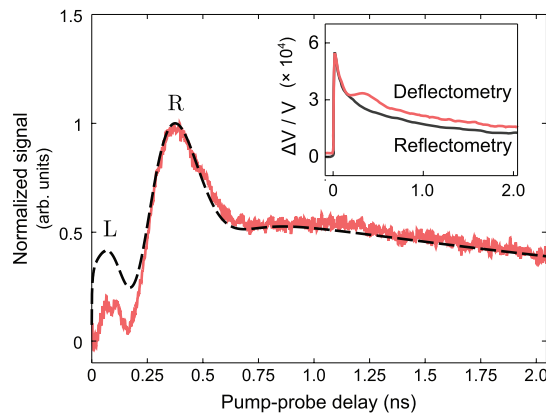
FIG. 6. (Color online) Comparison between corrected deflectometry signal (red plain line) and simulation of $\partial u_1/\partial x_2$ (black dashed line) for $d = 0.9$ μm. (Inset) Raw deflectometry signal (red plain line) and reflectometry signal (black line).

Sec. IV A. Figure 7 shows this comparison for pump-probe distances varying from 2.6 μm to 6.2 μm.

As the previous deflectometric measurements, skimming and Rayleigh waves are clearly visible on experimental signals. The amplitudes of the data plotted on Fig. 7 are normalized to facilitate the discussion. Good agreement with calculations is observed for the lowest d values. However, as d increases, an additional contribution to $\Delta V/V$ appears in addition to the contribution from u_1. In the case where pump and probe spots are superimposed (as modeled in Ref. 16), the probe beam is not deflected by the surface motion owing

to axial symmetry of the laser beams. This is not the case anymore when $d \neq 0$, and deflection of the probe beam occurs as a SAW propagates through the probe focal spot. This deflection modifies the probe power transmitted by the iris, adding a deflectometry contribution (proportional to the local slope $\partial u_1/\partial x_2$) to the BDD contribution (proportional to the normal displacement u_1). The amplitude of the deflectometric contribution reaches a plateau when the Rayleigh wave is probed outside the region heated by the pump spot, that is after a ≈ 2 μm propagation distance in our case.

In order to separate these two contributions, the BDD setup can be modified to optimize the vertical sample position x_1 with respect to the probe waist.[16] Indeed, setting the sample at the exact waist position would cancel the contribution of the normal displacement u_1 and only a deflection contribution would be measured. This property of the BDD technique should allow the simultaneous measurement of both the normal displacement u_1 and the local slope $\partial u_1/\partial x_2$ from BDD signals measured for different sample positions.

V. SUMMARY AND PERSPECTIVES

In conclusion, GHz SAWs have been generated on a semi-infinite titanium alloy using the absorption of femtosecond laser pulses and have been detected with two different optical schemes, the deflectometry and the BDD techniques. These techniques have been experimentally implemented by slightly modifying a conventional reflectometric setup, which makes them particularly straightforward compared to interferometric measurements. In order to analyze the optical generation and the detection of elastic waves on a semi-infinite medium, a semi-analytical model taking into account both the photothermal generation and the thermo-acoustic coupling has been developed.

As expected, deflectometry signals are proportional to the spatial derivative of the normal displacement, $\partial u_1/\partial x_2$. For pump-probe distances greater than the thermal length, these measurements are in remarkable agreement with the calculated $\partial u_1/\partial x_2$. Comparison between data and calculations has enabled characterization of the titanium sample and identification of skimming and Rayleigh waves. For smaller distances, good agreement is also achieved after subtraction of the photothermal contribution. Fine comparison between BDD measurements and calculations of the normal displacement reveals that BDD data sets may contain also a non-negligible contribution of deflection for large pump-probe distances.

Both experimental techniques and modeling can be applied to the characterization of anisotropic and viscoelastic halfspaces. In the future, these experimental techniques can be directly adapted to study the influence of submicrometric surface defects on GHz SAWs propagation or to tackle the study of interface acoustic waves between solids and transparent media, either solid or liquid.
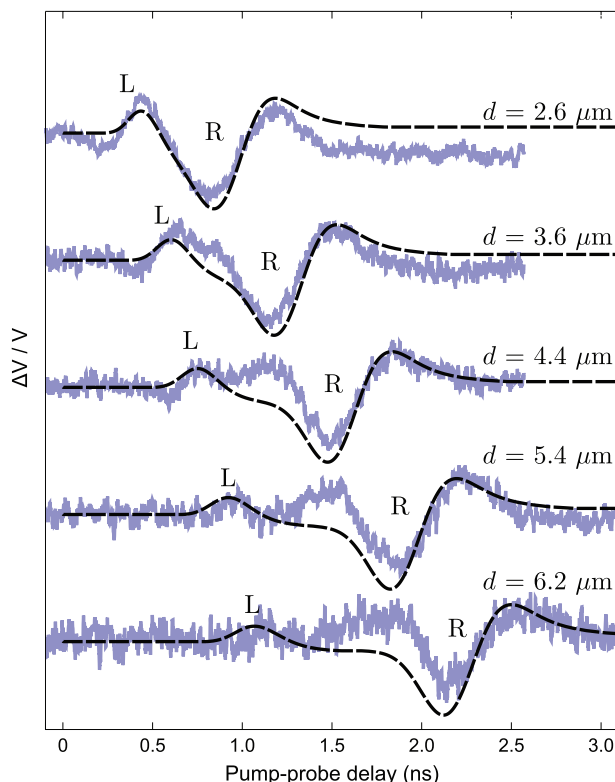

FIG. 7. (Color online) Comparison between normalized BDD measurements (light blue plain lines) and calculations of u_1 (black dashed lines) for pump-probe distances varying from $d = 2.6$ μm to $d = 6.2$ μm.

ACKNOWLEDGMENT

[1] D. M. Barnett and J. Lothe, Proc. R. Soc. London, Ser. A **402**, 135 (1985).

[2] N. E. Glass and A. A. Maradudin, J. Appl. Phys. **54**, 796 (1983).

[3] R. S. Edwards, S. Dixon, and X. Jian, J. Phys. D: Appl. Phys. **37**, 2291 (2004).

[4] N. Chigarev, T. Dehoux, C. Rossignol, B. Audoin, and V. Levin, J. Phys.: Conf. Ser. **92**, 012029 (2007).

[5] D. H. Hurley, R. Lewis, O. B. Wright, and O. Matsuda, Appl. Phys. Lett. **93**, 113101 (2008).

[6] V. Gusev and A. Karabutov, *Laser Optoacoustics* (American Institute of Physics, New York, 1993).

[7] V. Gusev, J. Appl. Phys. **107**, 114906 (2010).

[8] L. Dhar and J. A. Rogers, Appl. Phys. Lett. **77**, 1402 (2000).

[9] C. Thomsen, J. Strait, Z. Vardeny, H. J. Maris, J. Tauc, and J. J. Hauser, Phys. Rev. Lett. **53**, 989 (1984).

[10] C. Thomsen, H. T. Grahn, H. J. Maris, and J. Tauc, Phys. Rev. B **34**, 4129 (1986).

[11] T. Saito, O. Matsuda, M. Tomoda, and O. B. Wright, J. Opt. Soc. Am. B **27**, 2632 (2010).

[12] J. V. Knuuttila, P. T. Tikka, and M. M. Salomaa, Opt. Lett. **25**, 613 (2000).

[13] T. Tachizaki, T. Muroya, O. Matsuda, Y. Sugawara, D. H. Hurley, and O. B. Wright, Rev. Sci. Instrum. **77**, 043713 (2006).

[14] O. B. Wright and K. Kawashima, Phys. Rev. Lett. **69**, 1668 (1992).

[15] R. Salenbien, R. Côte, J. Goossens, P. Limaye, R. Labie, and C. Glorieux, J. Appl. Phys. **109**, 093104 (2011).

[16] N. Chigarev, C. Rossignol, and B. Audoin, Rev. Sci. Instrum. **77**, 114901 (2006).

[17] C. B. Scruby and L. E. Drain, in *Laser Ultrasonics: Techniques and Applications*, edited by P. Adam Hilger (IOP Publishing Ltd, Bristol and New York, 1990).

[18] J. E. Rothenberg, Opt. Lett. **13**, 713 (1988).

[19] M. A. Olmstead, N. M. Amer, S. Kohn, D. Fournier, and A. C. Boccara, Appl. Phys. A **32**, 141 (1983).

[20] B. Audoin, C. Rossignol, N. Chigarev, M. Ducousso, G. Forget, F. Guillemot, and M. Durrieu, Ultrasonics **50**, 202 (2010).

[21] A. J. Schmidt, X. Chen, and G. Chen, Rev. Sci. Instrum. **79**, 114902 (2008).

[22] As the position of the sample has not been set to optimize the BDD contribution to the reflectivity change, comparing BDD and deflectometry absolute amplitudes is not relevant.

[23] C. Bescond and M. Deschamps, J. Acoust. Soc. Am. **103**, 114 (1998).

[24] J. D. Achenbach, J. Mech. Phys. Solids **51**, 1885 (2003).

[25] B. Audoin, H. Meri, and C. Rossignol, Phys. Rev. B **74**, 214304 (2006).

[26] B. A. Auld, *Acoustic Fields and Waves in Solids* (R. E. Krieger Publishing Compagny, Malabar, FL, 1990), Vol. 1.

[27] T. Dehoux, N. Chigarev, C. Rossignol, and B. Audoin, Phys. Rev. B **77**, 214307 (2008).

[28] G. N. Watson, in *A Treatise on the Theory of Bessel Functions*, (Cambridge University Press, Cambridge, England, 1966).

[29] R. L. Weaver, W. Sachse, and K. Y. Kim, J. Appl. Mech. **63**, 337 (1996).

[30] T. Hsieh, E. Lindgren, and M. Rosen, Ultrasonics **29**, 38 (1991).

[31] M. Deschamps and G. Huet, Int. J. Non-Linear Mech. **44**, 469 (2009).